

# A new model of metal plasticity and fracture with pressure and Lode dependence

Yuanli Bai<sup>\*</sup>, Tomasz Wierzbicki

*Impact and Crashworthiness Lab, Massachusetts Institute of Technology,  
77 Massachusetts Avenue, Room 5-218, Cambridge, MA 02139, USA*

Received 28 June 2007; received in final revised form 28 August 2007  
Available online 14 September 2007

---

## Abstract

Classical metal plasticity theory assumes that the hydrostatic pressure has no or negligible effect on the material strain hardening, and that the flow stress is independent of the third deviatoric stress invariant (or Lode angle parameter). However, recent experiments on metals have shown that both the pressure effect and the effect of the third deviatoric stress invariant should be included in the constitutive description of the material. A general form of asymmetric metal plasticity, considering both the pressure sensitivity and the Lode dependence, is postulated. The calibration method for the new metal plasticity is discussed. Experimental results on aluminum 2024-T351 are shown to validate the new material model.

From the similarity between yielding surface and fracture locus, a new 3D asymmetric fracture locus, in the space of equivalent fracture strain, stress triaxiality and the Lode angle parameter, is postulated. Two methods of calibration of the fracture locus are discussed. One is based on classical round specimens and flat specimens in uniaxial tests, and the other one uses the newly designed butterfly specimen under biaxial testing. Test results of Bao (2003) [Bao, Y., 2003. Prediction of ductile crack formation in uncracked bodies. PhD Thesis, Massachusetts Institute of Technology] on aluminum 2024-T351, and test data points of A710 steel from butterfly specimens under biaxial testing validated the postulated asymmetric 3D fracture locus.

© 2007 Elsevier Ltd. All rights reserved.

**Keywords:** Pressure effect; Lode dependence; Yield surface; Fracture locus; Calibration method

---

---

<sup>\*</sup> Corresponding author.

E-mail address: [byl@mit.edu](mailto:byl@mit.edu) (Y. Bai).

## 1. Introduction

The classical J2 theory of metal plasticity assumes that the effect of hydrostatic pressure  $\sigma_m$  on plastic flow is negligible, and further assumes that the flow stress is independent of the third stress invariant of the stress deviator. For application to ductile fracture, these assumptions must be carefully examined. Ductile fracture is a local phenomenon and the state of stress and strain in potential fracture locations must be determined with great accuracy. Fracture initiation is often preceded by large plastic deformation and there are considerable stress and strain gradients around the point of fracture. In these situations, the infinitesimal J2 theory of plasticity is not accurate enough, and more refined plasticity models has to be introduced.

The soil and rock mechanics community has long recognized a need for incorporating the hydrostatic and deviatoric (Lode angle parameter) stress invariants into a constitutive descriptions (see for example [Bardet, 1990](#); [Menetrey and Willam, 1995](#)). More recently [Bigoni and Piccolroza \(2003\)](#) proposed a general failure surface for geomaterials in the space of principal stresses that reduces in limiting cases to the Tresca hexagon or the von Mises circle. The Sandia GeoModel ([Fossum and Brannon, 2006](#)) is also formulated in the space of three invariants. The developments in geomaterials was proceeding over the decades independently of metal plasticity with the latter lagging behind the former.

Based on an extensive experimental study, Richmond and Spitzig ([Richmond and Spitzig, 1980](#); [Spitzig and Richmond, 1984](#)) were first to demonstrate the effect of hydrostatic pressure on yielding of aluminum alloys. This conclusion has recently been confirmed by [Wilson \(2002\)](#), who studied notched 2024-T351 aluminum bars in tension. The concept of a shrinking yield surface with hydrostatic pressure was put forward independently by [Gurson \(1975\)](#) and later by [Needleman and Tvergaard \(1984\)](#) in their studies of ductile fracture by the nucleation, growth and coalescence of voids. The common shortcoming of these various theories of porous plasticity has been an ill-defined calibration procedure.

In general, the hydrostatic pressure is controlling the size of the yield surface while the Lode angle parameter is responsible for its shape. The determination of an adequate shape of the yield surface has become an issue in the sheet metal forming industry. It was found a long time ago that the von Mises plane stress ellipse does not lead to a correct prediction of the necking instability. There are an abundance of various modifications and generalizations of the plane stress yield curve to bring the prediction closer to reality ([Karafillis and Boyce, 1993](#); [Barlat et al., 1991, 1997, 2005](#); [Vegter and van den Boogaard, 2006](#)). However, most of the above theories included the effect of an in-plane anisotropy and the connection between the shape of yield condition and the Lode angle parameter has only been noticed recently. In particular, the effect of the Lode angle parameter (or the third deviatoric stress invariant) on plastic yielding has been studied by [Cazacu and Barlat \(2004\)](#), [Cazacu et al. \(2006\)](#), [Racherla and Bassani \(2007\)](#). Their models incorporate the difference in strength under compression and tension. They showed that the forming limit diagram of sheets was sensitive in that difference. However, their models did not have enough flexibility to predict plane strain yielding. Such a generalization is proposed in the present paper.

The paper is divided into two parts. The first part is concerned with a development of a more general plasticity model. Results of 21 tests on three groups of specimens are analyzed through a finite element simulation. It is shown that the parameters of the J2 plasticity model with power hardening rule, determined from one test, can not predict correctly the load–displacement responses in the all remaining tests. A new plasticity

model with correction for the hydrostatic pressure and the Lode parameter brings a perfect correlation with test results. Percentage-wise, the correction for the hydrostatic pressure is small. Physically, it could be attributed to the effect of hydrostatic pressure on metal crystal dislocations. The magnitudes of correction due to the deviatoric state parameter (Lode angle parameter) is large and in some cases reaches 20%. The effect of hydrostatic pressure is consistent with earlier finding of other authors (Richmond and Spitzig, 1980; Spitzig and Richmond, 1984; Wilson, 2002). The new yield surface is asymmetric in the space of principal stresses losing three planes of symmetry as compared to the Tresca yield condition with six plane of symmetry, so it is asymmetric in any of the Tresca's six symmetry planes.

The second part of the paper deals with the determination of the 3D locus of the fracture initiation points. The locus is determined experimentally from two types of test procedures. One is based on classical round specimens or flat specimens in uniaxial tests, and the other one uses a series of tests on a double curvature butterfly specimen subjected to biaxial loading under different combination of tension/shear and compression/shear. The test points are then fitted to a smooth surface which describes the dependence of the equivalent strain to fracture on the average stress triaxiality and the normalized third invariant of the deviatoric stress tensor (or Lode angle parameter). Again, it is shown that the best fit of test data is provided by a surface which is asymmetric with respect to the Lode angle parameter.

## 2. Characterization of the stress state

The extended metal plasticity model and the 3D fracture locus will be formulated in terms of three invariants of the stress tensor  $[\sigma]$ , defined respectively by

$$p = -\sigma_m = -\frac{1}{3}\text{tr}([\sigma]) = -\frac{1}{3}(\sigma_1 + \sigma_2 + \sigma_3), \quad (1)$$

$$q = \bar{\sigma} = \sqrt{\frac{3}{2}[S] : [S]} = \sqrt{\frac{1}{2}[(\sigma_1 - \sigma_2)^2 + (\sigma_2 - \sigma_3)^2 + (\sigma_3 - \sigma_1)^2]}, \quad (2)$$

$$r = \left(\frac{9}{2}[S] \cdot [S] : [S]\right)^{1/3} = \left[\frac{27}{2}\det([S])\right]^{1/3} = \left[\frac{27}{2}(\sigma_1 - \sigma_m)(\sigma_2 - \sigma_m)(\sigma_3 - \sigma_m)\right]^{1/3}, \quad (3)$$

where  $[S]$  is the deviatoric stress tensor,

$$[S] = [\sigma] + p[I], \quad (4)$$

$[I]$  is the identity tensor and  $\sigma_1$ ,  $\sigma_2$  and  $\sigma_3$  denote principal stresses. Note that the parameter  $p$  is positive in compression, but  $\sigma_m$  is positive in tension. It is convenient to work with the dimensionless hydrostatic pressure  $\eta$ , defined by

$$\eta = \frac{-p}{q} = \frac{\sigma_m}{\bar{\sigma}}. \quad (5)$$

The parameter  $\eta$ , often referred to as the triaxiality parameter, has been extensively used in the literature on ductile fracture (McClintock, 1968; Rice and Tracey, 1969; Hancock and Mackenzie, 1976; Mackenzie et al., 1977; Johnson and Cook, 1985; Bao, 2003). The second important parameter is the Lode angle  $\theta$ . The geometrical represent of Lode angle is

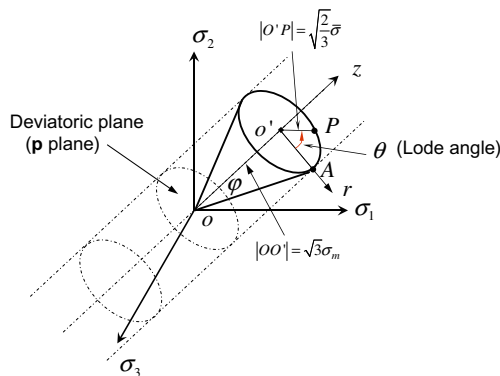


Fig. 1. Three types of coordinate system in the space of principal stresses.

shown in Fig. 1. The Lode angle  $\theta$  is related to the normalized third deviatoric stress invariant  $\xi$  (see Malvern, 1969; Xu and Liu, 1995) through

$$\xi = \left(\frac{r}{q}\right)^3 = \cos(3\theta). \quad (6)$$

Since the range of the Lode angle is  $0 \leq \theta \leq \pi/3$ , the range of  $\xi$  is  $-1 \leq \xi \leq 1$ . Furthermore, the Lode angle  $\theta$  can be normalized by

$$\bar{\theta} = 1 - \frac{6\theta}{\pi} = 1 - \frac{2}{\pi} \arccos \xi. \quad (7)$$

The range of  $\bar{\theta}$  is  $-1 \leq \bar{\theta} \leq 1$ . The parameter  $\bar{\theta}$  will be called the Lode angle parameter hereinafter. Now, all stress directions (or called loading conditions) can be characterized by the above defined set of parameters  $(\eta, \bar{\theta})$ . Various stress states encountered in “classical” specimens used for plasticity and fracture testing can be uniquely characterized by the above defined set of parameters  $(\eta, \bar{\theta})$ , as shown in Table 1. The analytical expressions for the stress triaxiality  $\eta$ , the parameter  $\bar{\theta}$  in terms of measurable quantities are all listed in Table 1.

Special attention is given to the plane stress state. It was shown by Wierzbicki and Xue (2005) that the condition  $\sigma_3 = 0$  uniquely relates the parameters  $\eta$  and  $\xi$  (or  $\bar{\theta}$ ) through

$$\xi = \cos \left[ \frac{\pi}{2} (1 - \bar{\theta}) \right] = -\frac{27}{2} \eta \left( \eta^2 - \frac{1}{3} \right). \quad (8)$$

A plot of Eq. (8) is shown in Fig. 2. Points corresponding to 10 types of “classical” specimens and tests are marked by circles. The function  $\bar{\theta}$  (Eq. (8)) has three roots corresponding to pure shear ( $\eta = 0$ ,  $\bar{\theta} = 0$ ) and the transverse plastic plane strain ( $\eta = \pm \frac{1}{\sqrt{3}}$ ,  $\bar{\theta} = 0$ ).

### 3. A new form of metal plasticity

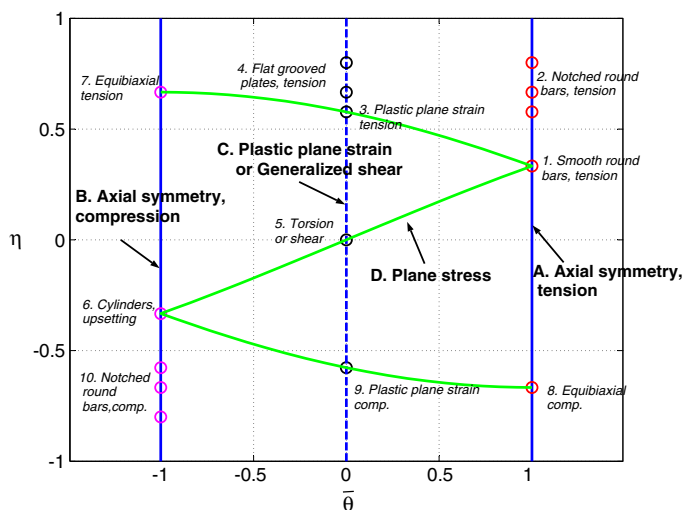
The plasticity theory to be developed in this section is valid under several assumptions. Firstly, the homogeneity and material isotropy are assumed. Secondly, the material is taken to be elastic–plastic with isotropic hardening. The extension to the combined isotropic/kinematic hardening could be made following the procedures suggested by Khan (for example Khan and Jackson, 1999). Finally, the plastic incompressibility is assumed.

Table 1

Ten types of classical specimens for plasticity and fracture calibration

No.	Specimen type	Analytical expressions for stress triaxiality $\eta^a$	The Lode angle parameter $\bar{\theta}$
1	Smooth round bars, tension	$\frac{1}{3}$	1
2	Notched round bars, tension (Bridgman, 1952)	$\frac{1}{3} + \sqrt{2} \ln \left( 1 + \frac{a}{2R} \right)$	1
3	Plastic plane strain, tension	$\frac{\sqrt{3}}{3}$	0
4	Flat grooved plates, tension (Bai et al., 2006b)	$\frac{\sqrt{3}}{3} \left[ 1 + 2 \ln \left( 1 + \frac{t}{4R} \right) \right]$	0
5	Torsion or shear	0	0
6	Cylinders, compression	$-\frac{1}{3}$	-1
7	Equi-biaxial plane stress tension	$\frac{2}{3}$	-1
8	Equi-biaxial plane stress compression	$-\frac{2}{3}$	1
9	Plastic plane strain, compression	$-\frac{\sqrt{3}}{3}$	0
10	Notched round bars, compression	$-\left[ \frac{1}{3} + \sqrt{2} \ln \left( 1 + \frac{a}{2R} \right) \right]$	-1

<sup>a</sup> In the expressions of  $\eta$ ,  $R$  is the radius of a notch or a groove,  $a$  is the radius of a round bar at the notch,  $t$  is the thickness of a flat grooved plate at the groove.

Fig. 2. Conceptual representation of the initial stress states on the plane of  $\eta$  and  $\bar{\theta}$ .

### 3.1. Effect of hydrostatic pressure on yield

The concept of pressure dependent yield condition goes back to Coulomb–Mohr, and Drucker and Prager (1952). This concept, originally developed for soil and granular materials, was shown more recently in a number of publications (Richmond and Spitzig, 1980; Brownrigg et al., 1983; Spitzig and Richmond, 1984; Brünig, 1999) to be applicable to metal plasticity. According to the above theories, the initial and current yield function is taken in this paper to be a linear function of the normalized pressure,  $\eta$ ,

$$\sigma_{\text{yld}} = \bar{\sigma}(\bar{\epsilon}_p) - \alpha I_1 = \bar{\sigma}(\bar{\epsilon}_p) \left[ 1 - \frac{3\alpha\sigma_m}{\bar{\sigma}(\bar{\epsilon}_p)} \right] = \bar{\sigma}(\bar{\epsilon}_p)(1 - 3\alpha\eta), \quad (9)$$

where  $I_1 = 3\sigma_m$  and  $\bar{\epsilon}_p$  is the equivalent plastic strain. The proportionality parameter  $\alpha$  should be calibrated from tests. In Eq. (9), the first strain hardening term,  $\bar{\sigma}(\bar{\epsilon}_p)$ , represents the stress–strain curve in zero hydrostatic pressure, for example in the torsion test. In practice, tensile tests of a smooth round bar or a dog-bone specimen are very commonly used to calibrate the stress–strain curve. Therefore, more generally, Eq. (9) can be rewritten as

$$\sigma_{yld} = \bar{\sigma}(\bar{\epsilon}_p, \eta_o)[1 - 3\alpha(\eta - \eta_o)] = \bar{\sigma}(\bar{\epsilon}_p)[1 - c_\eta(\eta - \eta_o)], \quad (10)$$

where  $\bar{\sigma}(\bar{\epsilon}_p)$  is material strain hardening function from the reference test, and  $\eta_o$  is the reference value of stress triaxiality from the reference test, for example,  $\eta_o = 1/3$  for smooth round bar tensile test,  $\eta_o = -1/3$  for cylindrical specimen compressive test,  $\eta_o = 0$  for torsion test and so on. Here,  $c_\eta$  is a material constant need to be calibrated, which represents the hydrostatic pressure effect on material plasticity. It should also be noted that the effect of pressure on plasticity does not have to be linear. Experimental data for ices showed a non-linear pressure effect (Karr et al., 1989). A linear function is proposed in this paper for metals.

The present concept of pressure dependent yield function for metals should not be confused with Gurson type of softening (Gurson, 1975; Needleman and Tvergaard, 1984) due to the nucleation, growth and linkage of voids. In a simple tensile test, it is difficult to tell what physical mechanism is responsible for the observed softening- the suppression of dislocation motion or the growth of material porosity with deformation. The physically based Eq. (10) explains a relative difference in the stress–strain curves obtained in tests with various stress triaxialities, which can be measured experimentally by a few simple tests. At the same time, the material softening in the GTN model (Needleman and Tvergaard, 1984) is an illusive concept because the reference state is the undamaged stress–strain curve for the matrix material, which can not be found from any simple tests. The reversibility of the softening is another issue even though (Spitzig and Richmond, 1984) did not address it directly. It is implicitly assumed that the dislocation suppression is reversible. This means that when in the loading process the hydrostatic pressure is brought back to the original value, the material will regain its initial strength. It is useful to design a test program involving a controlled change of the triaxiality to distinguish the two types of softening as discussed above. One such test could, for example, would involve two-stage tensile tests on notched round bars. After some plastic deformation the test is stopped and the gauge section of a specimen is re-machined to a larger radius. Such tests are being planned by the present authors.

### 3.2. Lode dependence

The dependence of the yield condition on the Lode angle parameter can best be explained by comparing the von Mises and Tresca yield condition. In the polar coordinate system, the equivalent stress becomes the radial coordinate while the circumferential coordinate is the Lode angle  $\theta$ . In the deviatoric stress plane, the von Mises yielding condition is represented by a circle. The Tresca yielding is a hexagon inscribed on the von Mises circle, as shown in Fig. 3.

To take the third deviatoric stress invariant into account, a new term considering the effect of the Lode angle is introduced into Eq. (10). The following yield criterion is proposed:

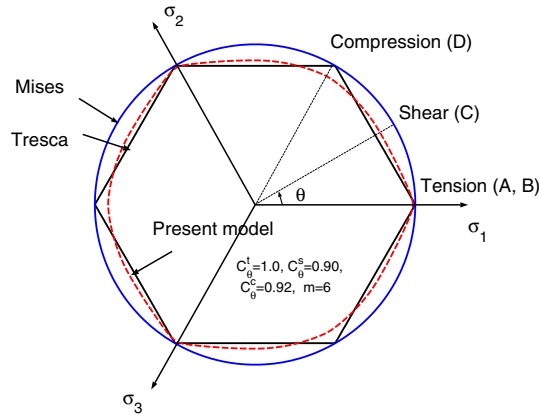


Fig. 3. Three yield loci in the deviatoric stress plane.

$$\sigma_{\text{yld}} = \bar{\sigma}(\bar{\epsilon}_p) [1 - c_\eta(\eta - \eta_0)] \left[ c_\theta^s + (c_\theta^{\text{ax}} - c_\theta^s) \left( \gamma - \frac{\gamma^{m+1}}{m+1} \right) \right], \quad (11)$$

where  $\gamma$  and  $c_\theta^{\text{ax}}$  are two parameters defined by

$$\gamma = \frac{\cos(\pi/6)}{1 - \cos(\pi/6)} \left[ \frac{1}{\cos(\theta - \pi/6)} - 1 \right] = 6.4641 [\sec(\theta - \pi/6) - 1], \quad (12)$$

$$c_\theta^{\text{ax}} = \begin{cases} c_\theta^t & \text{for } \bar{\theta} \geq 0, \\ c_\theta^c & \text{for } \bar{\theta} < 0. \end{cases} \quad (13)$$

Eq. (11) defines a class of function that define the shape of the yield surface. The term  $\cos(\theta - \pi/6)$  in the definition of the parameter  $\gamma$  represents the difference between von Mises and Tresca in the deviatoric stress plane, which is obtained from the geometrical construction by comparing the von Mises circle and the Tresca hexagon. After modification and normalization, the range of  $\gamma$  is  $0 \leq \gamma \leq 1$ , in which  $\gamma = 0$  is corresponding to plane strain or shear condition, and  $\gamma = 1$  is corresponding to axial symmetry. In Eq. (11), the leading term is linear with respect to the parameter  $\gamma$ , the higher order power term  $\left( \frac{\gamma^{m+1}}{m+1} \right)$  is introduced to make the yield surface smooth and differentiable with respect to Lode angle  $\theta$  around  $\gamma = 1$ . The parameter  $m$  is a non-negative integer. There are four material constants,  $c_\theta^t$ ,  $c_\theta^s$ ,  $c_\theta^c$  and  $m$ , need to be calibrated. The values of  $c_\theta^t$ ,  $c_\theta^s$ , and  $c_\theta^c$  are relative, and at least one of them is equal to unity. This depends on which type of reference test is used to calibrate the strain hardening function  $\bar{\sigma}(\bar{\epsilon}_p)$ . For example, if a smooth round bar tensile test is used, then  $c_\theta^t = 1$ ; if a torsion test is used, then  $c_\theta^s = 1$ ; if a cylinder specimen compressive test is used, then  $c_\theta^c = 1$ .

It can be proved that the postulated yield function (Eq. (11)) is smooth and differentiable. The convexity of yield surface is controlled by the ratios of three parameters  $c_\theta^t$ ,  $c_\theta^s$  and  $c_\theta^c$ . Compared with von Mises and Tresca yield conditions, this yield surface can be plotted in the deviatoric stress plane, as shown in Fig. 3. Examples of yield loci are shown in Fig. 4 for the case of plane stress.

By suitably choosing model parameters, some limiting cases are obtained. For example, assuming either  $c_\eta = 0$  and  $c_\theta^t = c_\theta^s = c_\theta^c = 1$  or  $m = 0$  gives the von Mises yield condition,

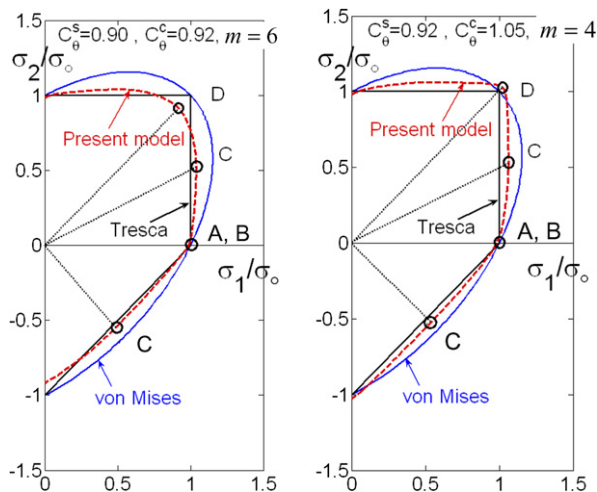


Fig. 4. Examples of yield locus for plane stress condition. (Here,  $c_\theta^t = 1$ , and the effect of hydrostatic pressure is dis-activated,  $c_\eta = 0$ ).

while taking  $c_\eta = 0$  and  $c_\theta^s = \sqrt{3}/2$ ,  $c_\theta^t = c_\theta^c = 1$ ,  $m = +\infty$  gives the Tresca yield criterion. If the parameter  $c_\eta \neq 0$  in above two cases, then one will get Drucker and Prager yield function (1952) and pressure-modified Tresca yield function. Most of metal plasticity theories assume that, in the deviatoric stress plane, the yield function is symmetric for uniaxial tension and uniaxial compression, which are corresponding to  $\bar{\theta} = 1$  and  $\bar{\theta} = -1$  respectively (for example, Tresca, 1864; Mises, 1913; Barlat et al., 1991; Karafillis and Boyce, 1993). This restriction can be removed in the present model by setting  $c_\theta^t \neq c_\theta^c$ . It should be noted that the flattening property of the von Mises ellipse, which is needed for right prediction of the Forming Limit Curves, was introduced by many authors in the space of principal stresses using non-quadratic yield function (Hosford, 1972; Karafillis and Boyce, 1993; Barlat et al., 1991, 1997), often under plane stress assumption. Vegter and van den Boogaard (2006) modeled the plane stress yield locus by fitting Brezier curves into four test points. Working on the deviatoric plane with the Lode angle dependence is another way of controlling the shape of the yield surface in a simple and elegant way.

### 3.3. The deviatoric associated flow rule

The yield surface, given by Eq. (11), can be visualized in the space of three principle stresses ( $\sigma_1, \sigma_2, \sigma_3$ ), see Fig. 5.

According to the conventional associated flow rule,

$$de_{ij}^{pl} = d\lambda \frac{\partial f}{\partial \sigma_{ij}}, \quad (14)$$

where the plastic potential is defined by

$$f = q - \bar{\sigma}(\bar{\epsilon}_p)[1 - c_\eta(\eta - \eta_0)] \left[ c_\theta^s + (c_\theta^{ax} - c_\theta^s) \left( \gamma - \frac{\gamma^{m+1}}{m+1} \right) \right], \quad (15)$$



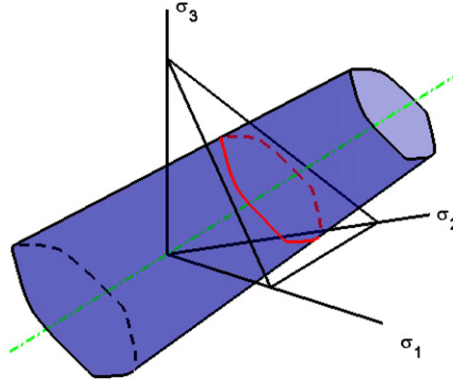


Fig. 5. A postulated 3D yield surface.

$d\lambda$  is the equivalent plastic strain increment, and  $q$  is defined by Eq. (2). To implement a yield function into finite element codes, a necessary step is to derive the expression for the normal direction (or flow direction) with respect to yield locus,  $\frac{\partial f}{\partial \sigma_{ij}}$ . From the yield function, Eq. (15), one can get

$$\begin{aligned} \frac{\partial f}{\partial \sigma_{ij}} = & \frac{\partial q}{\partial \sigma_{ij}} + \bar{\sigma}(\bar{\epsilon}^p) c_\eta \left[ c_\theta^s + (c_\theta^{\text{ax}} - c_\theta^s) \left( \gamma - \frac{\gamma^{m+1}}{m+1} \right) \right] \frac{\partial \eta}{\partial \sigma_{ij}} - \bar{\sigma}(\bar{\epsilon}^p) [1 - c_\eta (\eta - \eta_o)] \\ & \times (c_\theta^{\text{ax}} - c_\theta^s) (1 - \gamma^m) \frac{\partial \gamma}{\partial \sigma_{ij}}, \end{aligned} \quad (16)$$

where  $\frac{\partial q}{\partial \sigma_{ij}}$ ,  $\frac{\partial \eta}{\partial \sigma_{ij}}$  and  $\frac{\partial \gamma}{\partial \sigma_{ij}}$  can be expressed by the following equations.

$$\frac{\partial q}{\partial \sigma_{ij}} = \frac{3}{2q} s_{ij}, \quad (17)$$

$$\frac{\partial \eta}{\partial \sigma_{ij}} = \frac{1}{3q} \delta_{ij} - \frac{3\eta}{2q^2} s_{ij}, \quad (18)$$

$$\frac{\partial \gamma}{\partial \sigma_{ij}} = \left( \frac{3\sqrt{3}}{2 - \sqrt{3}} \right) \left( \frac{\tan(\theta - \pi/6)}{\cos(\theta - \pi/6)} \right) \frac{1}{q \sin 3\theta} \left( \frac{\delta_{ij}}{3} + \frac{\cos 3\theta}{2q} s_{ij} - \frac{3}{2q^2} s_{ik} s_{kj} \right). \quad (19)$$

Although the plasticity is pressure sensitive, experiments show that the plastic dilatancy of metals is negligible (Spitzig and Richmond, 1984). To satisfy the assumption of plastic incompressibility, the first term  $\frac{1}{3q} \delta_{ij}$  in Eq. (18) should be removed. Therefore, what is used in the present paper is a flow rule with *deviatoric associativity*, see Eq. (20), rather than the conventional associated flow rule, Eq. (16).

$$\begin{aligned} d\epsilon_{ij}^{pl} = & d\lambda \left\{ \frac{3}{2q} s_{ij} - \bar{\sigma}(\bar{\epsilon}_p) c_\eta \left[ c_\theta^s + (c_\theta^{\text{ax}} - c_\theta^s) \left( \gamma - \frac{\gamma^{m+1}}{m+1} \right) \right] \frac{3\eta}{2q^2} s_{ij} \right. \\ & - \bar{\sigma}(\bar{\epsilon}_p) [1 - c_\eta (\eta - \eta_o)] (c_\theta^{\text{ax}} - c_\theta^s) (1 - \gamma^m) \\ & \left. \times \left( \frac{3\sqrt{3}}{2 - \sqrt{3}} \right) \left( \frac{\tan(\theta - \pi/6)}{\cos(\theta - \pi/6)} \right) \frac{1}{q \sin 3\theta} \left( \frac{\delta_{ij}}{3} + \frac{\cos 3\theta}{2q} s_{ij} - \frac{3}{2q^2} s_{ik} s_{kj} \right) \right\}. \end{aligned} \quad (20)$$

Clearly, the presence of additional terms in Eq. (20) indicate that the direction of plastic flow is normal to the yield surface in the deviatoric plane but not to von Mises yield surface. In this issue, the present formulation can be classified as an intermediate flow rule between the non-associated flow rule and the conventional “fully” associated one. (It should be noted that if this model is used to model other non-metallic porous materials, which are plastic compressible, then a fully associated flow rule as previous stated is necessary). This new form of metal plasticity has been implemented into Abaqus user material subroutine VUMAT using the classical mapping return algorithm. The following numerical simulations are run with the material subroutine.

#### 4. Experimental calibration of 2024-T351 aluminum

A power function is introduced to describe the isotropic stain hardening for metal plasticity.

$$\bar{\sigma}(\bar{\epsilon}_p) = A(\epsilon_o + \bar{\epsilon}_p)^n \quad \text{for } \bar{\sigma} \geq \sigma_y, \quad (21)$$

where  $\epsilon_o$  is the first yield strain. There are nine parameters,  $A$ ,  $\epsilon_o$ ,  $n$ ,  $c_\eta$ ,  $\eta_o$ ,  $c_\theta^l$ ,  $c_\theta^s$ ,  $c_\theta^c$ , and  $m$ , in the present plasticity model. To validate and calibrate the model, four types of tests are required. The first test is the smooth round bar tensile test, from which the baseline stress–strain curve (parameters:  $A$ ,  $\epsilon_o$  and  $n$ ) can be determined. Also, the reference parameters are uniquely defined:  $\eta_o = 1/3$  and  $c_\theta^l = 1$ . The second test is the notched round bars tensile test. Introducing a geometric notch to a smooth round bar increases the hydrostatic pressure in the materials inside the neck. Wilson (2002) conducted this type of test on aluminum 2024-T351, and calibrated the pressure effect on metal plasticity, but the effect of Lode angle was not taken into account. The third test is the tensile test of flat grooved plates, which can be used to calibrate the parameter  $c_\theta^s$ . The fourth test is the cylindrical specimens’ upsetting test, which can be used to calibrate the last two parameters  $c_\theta^c$  and  $m$ . The corresponding stress states of these four types of tests are also respectively marked as A, B, C and D in Fig. 3. The analysis and a description of experimental study of the first three types of tests were described in the earlier report (Bai et al., 2006b) in detail. In this paper, emphasis is put on the numerical simulation study and plastic model calibration.

##### 4.1. Smooth and notched round bars tensile tests

Smooth round bar tensile tests were used to calibrate the stress–strain curve. There are three steps involved. Firstly, the engineering stress–strain curve  $\sigma_E(\epsilon_E)$  is obtained from the force–displacement curve  $P(u)$  recorded during the test. Secondly, the true stress–strain curve  $\bar{\sigma}(\bar{\epsilon})$  is calculated from the engineering stress–strain curve using the classical transformation law,  $\bar{\sigma} = \sigma_E(1 + \epsilon_E)$  and  $\bar{\epsilon} = \ln(1 + \epsilon_E)$ . In this step, only the data point before specimen necking can be used because the transformation equations are valid only up to necking initiation. Approximately, one can take the peak point of the force–displacement curve as the necking initiation point. Thirdly, a power function (Eq. (21)) is used to fit the true stress–strain curve obtained from the test. This curve is then extrapolated to get the approximate true stress–strain curve after necking.

Two methods are available to determine more precisely the true stress–strain curve after necking. If the continuous measurements of the neck geometry are available, then the Bridgman correction is applicable. Alternatively, the inverse method could be used in

which the stress–strain curve after necking is adjusted to get good agreement of the measured force–displacement curve. For the present material, the neck was not deep and it was not necessary to adjust the stress–strain curve after necking.

A group of tensile tests of smooth and notched round bars were conducted, refer to Fig. 6. The diameter of smooth round bar specimens is 9 mm. For notched round bar specimens, the diameter of the minimal cross-section is 8 mm, and two radii of notches are assigned, equal to 12 mm and 4 mm, respectively. The diameters in specimens shoulder are all equal to 15 mm, and the length of gauge section for this group of specimens is 25.5 mm. The selected material is aluminum 2024-T351. To diminish a possible effect of material anisotropic, all the specimens discussed in this paper are machined from the rolling direction (or 90° direction) of a same material block. Furthermore, Bao (2003) has shown that the effect of anisotropy of 2024-T351 aluminum alloy is negligible. Two to four tests are conducted for each case.

The stress–strain curve was calibrated from a smooth round bar tensile test, so  $\eta_0 = 1/3$ . To calibrate the pressure dependence coefficient  $c_\eta$ , the finite element models of the specimens were constructed with the Lode angle terms switched off. Round bar specimens are discretized by 4-node axisymmetric elements. Finite element models of Abaqus/explicit are built, in which the user material subroutine VUMAT is used. The measured force–displacement curves are shown in Figs. 7 and 8. In order to study possible mesh dependency, calculations were run using fine (0.1 mm) and coarse (0.2 mm) meshes. The maximal difference of the force–displacement response was less than 0.5%, meaning that the finite element solution was convergent. All the results presented in this paper use the fine mesh size. From Figs. 7 and 8, one can see that without any corrections, the force–displacement response of the smooth round bar simulation agrees with the experimental results very well, but the notched round bar simulations over-predict the force–displacement curves about 3–6%. Similar reduction in the material strength were also reported by Brünig (1999) and Kuroda (2004). The reason is that the material points inside a notched round bar are subjected to higher pressure than the smooth round bar. This phenomenon shows the effect of hydrostatic pressure on stress–strain curve. By changing the coefficient  $c_\eta$  iteratively, a value of  $c_\eta = 0.09$  is obtained, which makes the force–displacement curves



Fig. 6. A group of smooth and notched round bar specimens.

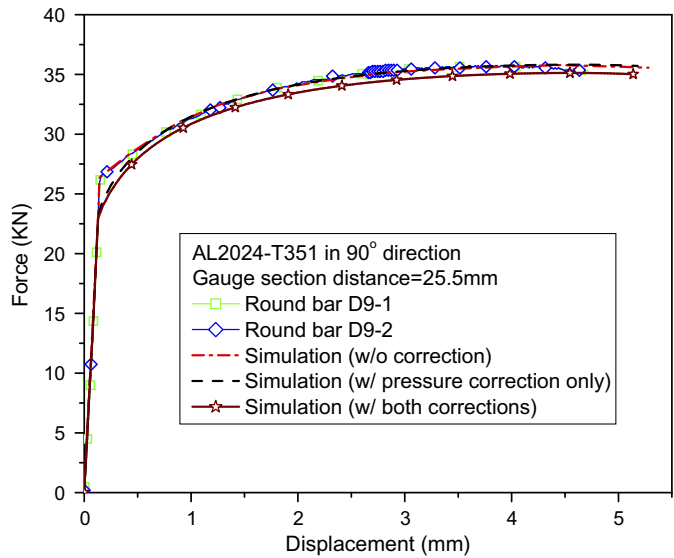


Fig. 7. A comparison of force–displacement curves between experimental results and simulation results: smooth round bars, diameter = 9 mm.

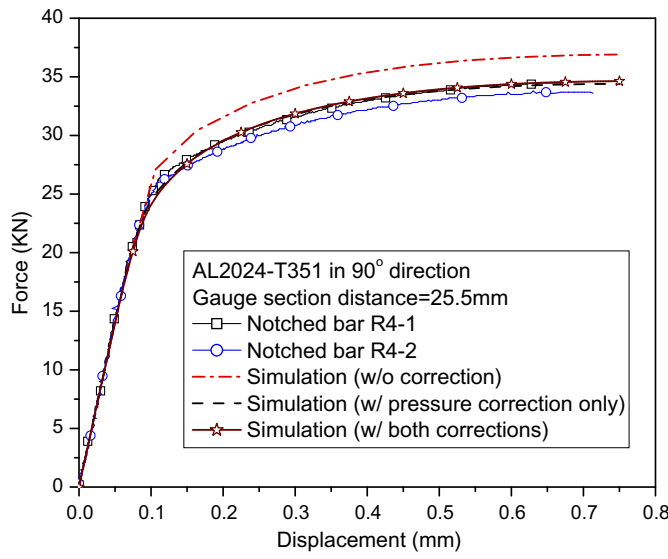


Fig. 8. A comparison of force–displacement curves between experimental results and simulation results: notched round bars, diameter = 8 mm, notch radius = 4 mm.

agree with the experiment results (the errors become less than 0.8%), as shown in Figs. 7 and 8. A comparison was also done for the case with notch radius equal to 12 mm, but for the sake of brevity, it is not shown in this paper (see Bai et al., 2006b) for a complete analysis.

The calibrated pressure effect in Wilson's paper (Wilson, 2002) gives  $\alpha = 0.03$  for apparently the same material. One can see that the present method to calibrate  $c_\eta$  is different from the one Wilson suggested, but the result is similar.

#### 4.2. Flat grooved plates tensile tests

Another group of tensile tests of flat grooved plates, as shown in Fig. 9, were conducted as described in detail in the earlier report (Bai et al., 2006b). The width of the specimens is 50 mm. Four types of radii of the grooves are machined: 12.7 mm, 3.97 mm, 2.38 mm, and 1.59 mm. Two nominal thicknesses in the minimal cross-section are assigned to these specimens:  $t = 2.11$  mm is assigned to the one with 1.59 mm groove radius, and  $t = 1.6$  mm is assigned to the other ones. The plate thicknesses at the specimens shoulder are all equal to 5 mm, and the length of gauge section for this group of specimens is 25 mm. The flat grooved specimen has a same range of stress triaxiality with that of notched round bars, but the corresponding values of the Lode angle parameter  $\bar{\theta}$  are different. This feature gives a direct way to see the effect of the Lode angle parameter on metal plasticity. Again, the finite element simulation of physical tests is needed to find the remaining parameters.

The flat grooved specimens are discretized by 8-node solid elements with mesh size 0.1 mm. Finite element models are built and run by Abaqus/explicit with the material user subroutine. Due to symmetry condition, 1/8 of a full scale model is used. Comparisons of force–displacement curves between numerical simulations and experimental results of the case with the sharpest groove notch are illustrated in Fig. 10. Without any corrections, one can see large differences between numerical simulations and experiments in force responses from these figures (the errors are about 14–19%). If only a hydrostatic pressure effect ( $c_\eta = 0.09$ ) is introduced, the differences between numerical simulations and experiments becomes smaller but can not be eliminated (the errors become 12–16%). Here, it is found that the pressure effect correction is not enough, and the Lode angle parameter effect should also be taken into account. By changing the coefficient  $c_\theta^s$  iteratively, a value of  $c_\theta^s = 0.855$  is obtained, which makes the force–displacement curves agree well with the experimental results (the errors now become less than 2%), as shown in Fig. 10. The comparison was done for all four radii of the groove, but for the sake of brevity, only the result



Fig. 9. A group of flat grooved specimens.

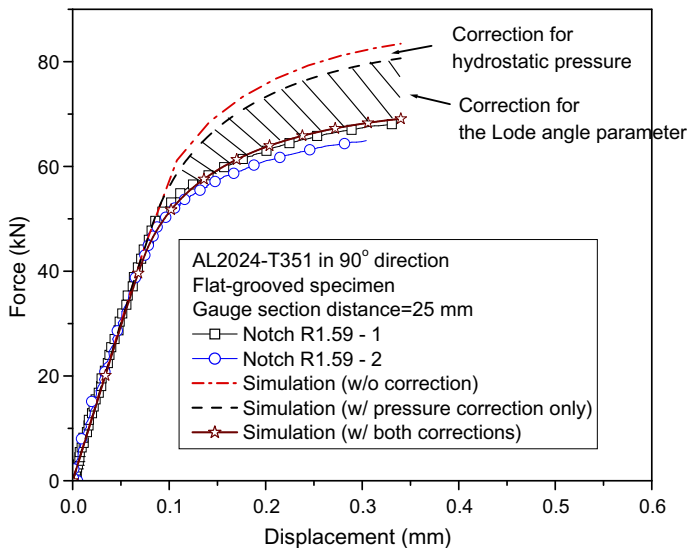


Fig. 10. A comparison of force–displacement curves between experimental results and simulation results: flat grooved specimens, thickness = 2.11 mm, groove radius = 1.59 mm.

for the sharpest groove is shown (see Bai et al., 2006b for a complete analysis). From these two groups of tests, it can be concluded that the corrections of both the hydrostatic pressure effect and the Lode dependence are necessary for aluminum 2024-T351.

#### 4.3. Cylindrical specimens upsetting tests

The remaining two parameters  $c_\theta^c$  and  $m$  are found from the upsetting tests. Round bars' tensile tests and flat grooved plates' tensile tests correspond to loading conditions of  $\bar{\theta} = 1$  and  $\bar{\theta} = 0$  respectively. The loading condition of cylindrical specimens in the upsetting test is  $\bar{\theta} = -1$  and  $\eta = -1/3$ . Since the pressure effect on plasticity is already calibrated in the previous two groups of tests, the upsetting tests will help to determine the shape of the yield surface at  $\bar{\theta} = -1$ . To check whether the yield surface is symmetric with respect to the Lode angle parameter  $\bar{\theta}$  or not, a group compressive tests on cylindrical specimens were conducted. The diameters of the specimens were 8 mm, and two heights (6 mm and 11.25 mm) were assigned to two types of cylinders, as shown in Fig. 11.

The cylindrical specimens are discretized by 4-node axisymmetric elements with mesh size 0.1 mm. Finite element models are built and run by Abaqus/explicit with the material user subroutine. Because the friction coefficient ( $\mu$ ) between specimens and the platform of the testing machine is unknown, the friction coefficient is adjusted iteratively in the simulation to make the final deformed shape of specimens agree with the experimental results. Comparisons of the force–displacement curves between numerical simulations and experimental results were made for all tests, and a typical result is shown in Fig. 12. The value of  $\mu$  used in the simulation is also provided in the figure. It is found that, using simply the power hardening law, there is a difference between numerical simulations and experimental results (the errors are about 6–10%). Adjusting the parameters,  $c_\theta^c$  and  $m$ , iteratively in the numerical simulation, the set of parameter  $c_\theta^c = 0.90$  and  $m = 6$  is obtained, which



Fig. 11. Two groups of cylindrical specimens for upsetting tests.

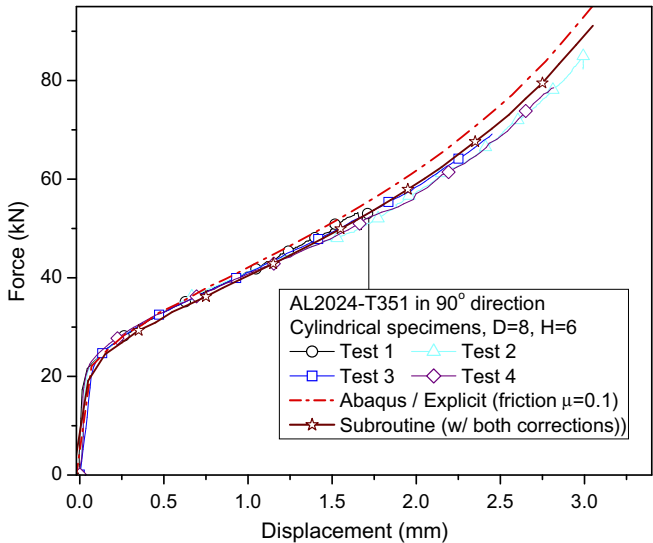


Fig. 12. A comparison of force–displacement curves between experimental results and simulation results: cylindrical specimens, diameter = 8 mm, height = 6 mm.

makes the force–displacement curves agree well with the experimental ones (the errors become less than 2.5%), see Fig. 12. This proves that the yield surface of aluminum 2024-T351 is not symmetric because of  $c_{\theta}^t \neq c_{\theta}^c$ . In summary, the calibrated plasticity model parameters of aluminum 2024-T351 as listed in Table 2. This completes the calibration process of plastic behavior.

Table 2  
Calibrated material properties of aluminum 2024-T351 (rolling direction)

Basic material properties	Pressure effect and lode dependence constants
Density $\rho = 2.7e + 3 \text{ kg/m}^3$	$\eta_o = 1/3$
Poisson's ratio = 0.3	$c_{\eta} = 0.09$
Young's modulus $E = 7.115e + 5 \text{ (MPa)}$	$c_{\theta}^t = 1.0$
Yield stress $\sigma_y = 370 \text{ (MPa)}$	$c_{\theta}^c = 0.855$
Stress–strain curve $\bar{\sigma} = 908(0.0058 + \bar{\epsilon}_p)^{0.1742} \text{ (MPa)}$	$c_{\theta}^s = 0.90$
	$m = 6$



## 5. The asymmetric 3D fracture locus

Compared with the strain hardening, the hydrostatic pressure effect on metal plasticity is relatively small. However, the hydrostatic pressure is one of the most important parameters that controls material ductility. The equivalent plastic strain to fracture ( $\bar{\epsilon}_f$ ) is widely used to measure material ductility. Theoretical analysis (McClintock, 1968; Rice and Tracey, 1969) and numerous experimental studies (Hancock and Mackenzie, 1976; Mackenzie et al., 1977; Johnson and Cook, 1985; Bao, 2003) have proved that the fracture strain increases when the hydrostatic pressure increases. Wilkins et al. (1980) was first to introduce the effect of deviatoric stress ratio  $A_s$ , which is related to Lode angle parameter  $\bar{\theta}$  or the normalized third stress invariant  $\xi$ , on ductile fracture.

$$\bar{\epsilon}_f = w_1(p)w_2(A_s) = g_1(p)g_2(\bar{\theta}) = h_1(\eta)h_2(\xi). \quad (22)$$

Furthermore, the function  $g_2$  was taken to be symmetric with respect to the parameter  $\bar{\theta}$ . In this model as well as its subsequent applications (Kamoulakos et al., 2003; Xue, 2007), the dependence of the fracture locus on the parameter  $\eta$  and  $\bar{\theta}$  was assumed to be separable (see Eq. (22)). As an extension of Wilkin's model and Johnson–Cook's model, Wierzbicki and Xue (2005) postulated a non-separable but symmetric 3D fracture locus in the space of stress triaxiality and the normalized third stress invariant  $\xi$ ,  $\bar{\epsilon}_f = \hat{\epsilon}_f(\eta, \xi)$ , which is shown in Fig. 13.

However, the assumptions of the separable form and symmetry of the fracture locus might be too restrictive, and they were not based on the experimental evidence. Tests have shown that the effect of the third deviatoric stress invariant on ductile fracture initiation becomes weak in the high range of pressures or high stress triaxiality region (Hancock and Brown, 1983; Bai et al., 2006b). In low stress triaxiality region, a cylinder's upsetting test (corresponding to the loading condition  $\eta = -1/3$  and  $\bar{\theta} = -1$ ) will give a quick check on the effect of the third deviatoric stress invariant. A common practice in the literatures is to extrapolate the fracture locus determined from high stress triaxiality region to the low stress triaxiality region. If the fracture locus is symmetric with respect to  $\bar{\theta}$  as postulated by Wilkins et al., Wierzbicki and Xue (as is shown in Fig. 13), then the fracture strain of cyl-

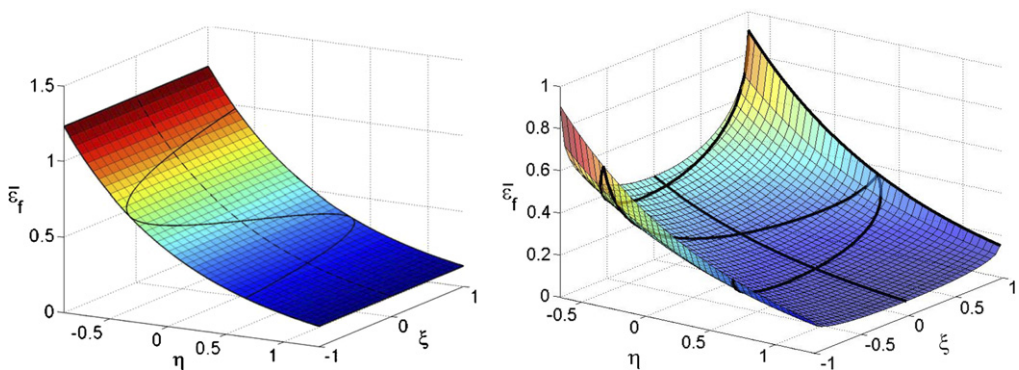


Fig. 13. The fracture locus independent of  $\xi$  (or  $\bar{\theta}$ ) postulated by Johnson and Cook (1985) (left), and a 3D symmetric fracture locus accounting for  $\xi$  postulated by Wierzbicki and Xue (Wierzbicki and Xue, 2005; Wierzbicki et al., 2005b) (right).



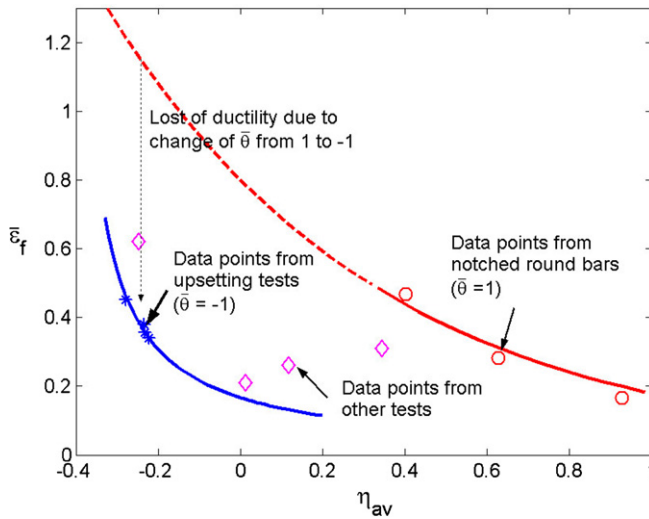


Fig. 14. A new interpolation of Bao's data points of aluminum 2024-T351 (experimental data from Bao's tests (Bao, 2003)).

inders upsetting tests (corresponding to  $\bar{\theta} = -1$ ) should lay on the extrapolated curve of fracture locus calibrated by notched round bars tensile tests (corresponding to the loading condition  $\eta \geq 1/3$  and  $\bar{\theta} = 1$ ).

Bao (2003), Bao and Wierzbicki (2004) designed a series of tests to calibrate the fracture strain in the entire range of stress triaxiality. It is clear from Fig. 14 that the fracture strains of upsetting tests are far below the extrapolated curve. In view of mounting experimental evidence, it can be hypothesized that the loss of ductility in upsetting tests are due to the Lode angle parameter  $\bar{\theta}$ , which changes from 1 to  $-1$ . The phenomenon is confirmed by more recent tests conducted by El-Magd et al. (2001), who performed similar tests on AlMgSi.F31 alloy.

As an extension of the 2D fracture locus, the 3D fracture locus is constructed in the space of  $(\bar{\epsilon}_f, \eta, \bar{\theta})$ . Since the effect of the Lode angle parameter on fracture strain is not uniform for different stress triaxialities, it is proposed to construct the fracture locus based on the boundary limits. There are three limiting cases in the fracture locus:  $\bar{\epsilon}_f^{(-)}$  (corresponding to axial symmetry in deviatoric compression,  $\bar{\theta} = -1$ ),  $\bar{\epsilon}_f^{(0)}$  (corresponding to plastic plane strain or generalized shear,  $\bar{\theta} = 0$ ), and  $\bar{\epsilon}_f^{(+)}$  (corresponding to axial symmetry in deviatoric tension,  $\bar{\theta} = +1$ ). Tests should tell which bound limit is the upper limit and which is the lower limit. There are many possibilities. Experimental data on geological materials from Han and Chen (1985) show that  $\bar{\epsilon}_f^{(-)} > \bar{\epsilon}_f^{(+)}$ , but others data from Bardet (1990) suggest that  $\bar{\epsilon}_f^{(+)} > \bar{\epsilon}_f^{(-)}$ . Theoretical analysis based on Gurson's model by Gao and Kim (2006) and cubic cell unit by Zhang et al. (2001) show that  $\bar{\epsilon}_f^{(+)} > \bar{\epsilon}_f^{(-)}$  in high stress triaxiality region. It is also possible that these three curves will intersect when projecting the 3D surface into the plane of the equivalent fracture strain and stress triaxiality. Based on the theory of McClintock (1968) and Rice and Tracey (1969) on void growth, the exponential function for the effect of stress triaxiality on fracture strain is used. Regarding the effect of  $\bar{\theta}$  on fracture locus, a parabolic function is proposed. Hence, the following form of the fracture locus is postulated,

$$\begin{aligned}
 \hat{\epsilon}_f(\eta, \bar{\theta}) &= \left[ \frac{1}{2} (\hat{\epsilon}_f^{(+)} + \hat{\epsilon}_f^{(-)}) - \hat{\epsilon}_f^{(o)} \right] \bar{\theta}^2 + \frac{1}{2} (\hat{\epsilon}_f^{(+)} - \hat{\epsilon}_f^{(-)}) \bar{\theta} + \hat{\epsilon}_f^{(o)} \\
 &= \left[ \frac{1}{2} (D_1 e^{-D_2 \eta} + D_5 e^{-D_6 \eta}) - D_3 e^{-D_4 \eta} \right] \bar{\theta}^2 + \frac{1}{2} (D_1 e^{-D_2 \eta} - D_5 e^{-D_6 \eta}) \bar{\theta} \\
 &\quad + D_3 e^{-D_4 \eta}.
 \end{aligned} \tag{23}$$

In this new fracture locus function, six parameters,  $D_1$ ,  $D_2$ ,  $D_3$ ,  $D_4$ ,  $D_5$ , and  $D_6$  need to be calibrated. The term  $D_1 e^{-D_2 \eta}$  gives the  $\bar{\epsilon}_f^{(+)}$  limit of the fracture locus,  $D_3 e^{-D_4 \eta}$  gives the  $\bar{\epsilon}_f^{(o)}$  limit of the fracture locus, and  $D_5 e^{-D_6 \eta}$  gives the  $\bar{\epsilon}_f^{(-)}$  limit of the fracture locus. It should be noted that in this paper, the Lode angle parameter  $\bar{\theta}$ , instead of the normalized third deviatoric stress invariant  $\xi$ , will be used to formulate the fracture locus. A geometrical representation of the new fracture locus in the 3D space is shown in Fig. 15. Generally speaking,  $\bar{\epsilon}_f^{(+)} \neq \bar{\epsilon}_f^{(-)}$ , which implies the asymmetry. It should be noted that a function convexity is not necessary in strain (or stress) space for the 3D fracture locus.

Many special cases of the fracture loci can be recovered from the above general function. For example, by requiring symmetry with respect to  $\bar{\theta}$ ,  $\bar{\epsilon}_f^{(+)} = \bar{\epsilon}_f^{(-)} = \bar{\epsilon}_f^{(ax)}$ , Eq. (23) becomes

$$\hat{\epsilon}_f(\eta, \bar{\theta}) = [\hat{\epsilon}_f^{(ax)} - \hat{\epsilon}_f^{(o)}] \bar{\theta}^2 + \hat{\epsilon}_f^{(o)}, \tag{24}$$

which is similar to the Xue–Wierzbicki symmetric fracture locus. It should be noted that neither Eq. (23) nor Eq. (24) is of a separable form in  $\eta$  and  $\bar{\theta}$  as assumed by Wilkins et al. (1980), Kamoulakos et al. (2003) and Xue (2007). If the effect of  $\bar{\theta}$  on fracture locus is taken away,  $\bar{\epsilon}_f^{(ax)} = \bar{\epsilon}_f^{(o)}$ , Eq. (24) becomes

$$\hat{\epsilon}_f(\eta, \bar{\theta}) = \hat{\epsilon}_f^{(o)} = D_3 e^{-D_4 \eta}, \tag{25}$$

which is identical to the Rice–Tracey’s fracture locus (Rice and Tracey, 1969) and also to a reduced form of Johnson–Cooks criteria (Johnson and Cook, 1985).

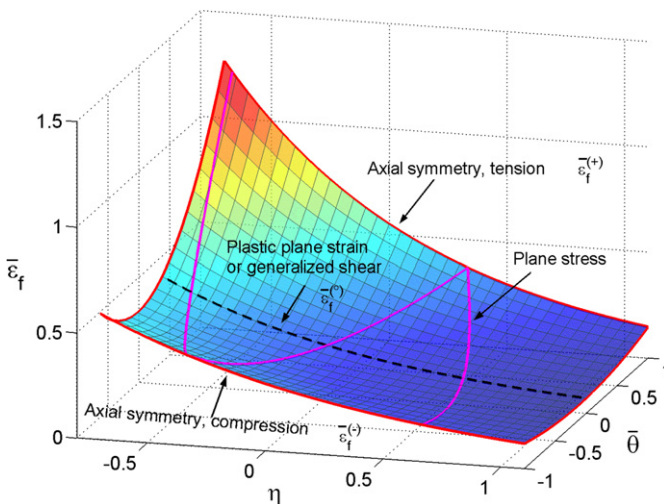


Fig. 15. A newly postulated 3D asymmetric fracture locus.

## 6. Fracture locus calibration

### 6.1. Fracture locus calibration using “classical” specimens

There are six parameters in Eq. (23), so at least six different tests need to be performed to calibrate the material for fracture. Ten types of classical specimens and tests are listed in Table 1 and also shown in Fig. 2. From this table, it is suggested to choose the first seven types of specimens to calibrate the fracture locus.

An emphasis is put on two groups of tests, the smooth and notched round bars tensile tests (No. 1 and 2 in Table 1,  $\bar{\theta} = 1$ ) and the flat grooved plates tensile tests (No. 3 and 4,  $\bar{\theta} = 0$ ). In Section 4, these two groups of tests were used to calibrate the new form of metal plasticity. These two groups of tests are also very useful to fracture locus calibration because the tests on smooth and notched round bars will give  $\bar{\epsilon}_f^{(+)}$ , and the tests on flat grooved specimens will give  $\bar{\epsilon}_f^{(o)}$ . Regarding the third bound limit,  $\bar{\epsilon}_f^{(-)}$ , cylinders upsetting test (No. 6) and equi-biaxial tension test (No. 7) can be used.

For thin metal sheets, it is difficult to machine round specimens, so the flat dog-bone specimen tensile test (corresponding to No. 1 in Table 1), plane strain tension (No. 3), flat grooved plates tensile tests (No. 4), shear test (No. 5), and equi-biaxial tension test (No. 7) are suggested.

A Matlab code is written to optimize the data points of tests to get the best surface fitting. An optimization function is chosen as to minimize the average error, see the following equation:

$$\text{Min}_{(D_1, D_2, \dots, D_6)} (\text{Error})_{\text{av}} = \text{Min}_{(D_1, D_2, \dots, D_6)} \left[ \frac{1}{N} \sum_{i=1}^N \left| \frac{\hat{\epsilon}_f(\eta_i, \bar{\theta}_i) - \bar{\epsilon}_{f,i}}{\bar{\epsilon}_{f,i}} \right| \right]. \quad (26)$$

The curve fitting result of Rice–Tracey criteria (Eq. (25)) is used as the initial values of all three limits for optimization searching process in the Matlab code. After many runs, the  $\bar{\epsilon}_f^{(+)}$  limit,  $\bar{\epsilon}_f^{(o)}$  limit and  $\bar{\epsilon}_f^{(-)}$  limit of the fracture locus are obtained, and the 3D fracture locus is constructed.

The above procedure is first applied to characterize fracture of 2024-T351 aluminum alloy. Bao (2003) designed and performed 14 tests on 2024-T351 aluminum for fracture locus calibration. These tests included smooth/notched round bar tensile tests, cylindrical specimens upsetting tests, plane strain test, shear test and so on. The fracture data points of all 14 tests can be found in Table 2 of Ref. (Wierzbicki et al., 2005b), and 10 of them is also shown in Fig. 14. It should be noted that in this table and throughout the present paper, the fracture strains were evaluated using a combined experimental/numerical method. The calculated strain at the fracture initiation point corresponding to the measured displacement to fracture is understood as a fracture strain. As a first iteration, the parameters of the Rice–Tracy’s criteria was determined, see the following equation:

$$\bar{\epsilon}_f = 0.3445e^{-0.4109\eta}. \quad (27)$$

Taking the corresponding cylindrical surface as an initial value of the optimization process, the full 3D fracture locus was found in the form of the following equation:

$$\begin{aligned} \hat{\epsilon}_f(\eta, \bar{\theta}) = & \left[ \frac{1}{2} (0.5862e^{-1.3576\eta} + 0.4859e^{-0.700\eta}) - 0.2170e^{-0.0400\eta} \right] \bar{\theta}^2 \\ & + \frac{1}{2} (0.5862e^{-1.3576\eta} - 0.4859e^{-0.700\eta}) \bar{\theta} + 0.2170e^{-0.0400\eta}. \end{aligned} \quad (28)$$

If a symmetric fracture locus (Eq. (24)) is used in surface fitting process, then a symmetric fracture locus is obtained as follows:

$$\bar{\epsilon}_f = (0.4534e^{-0.7788\eta} - 0.2147e^{-0.0400\eta})\bar{\theta}^2 + 0.2147e^{-0.0400\eta}. \quad (29)$$

The average error of all 14 test data is reduced from 21.4% of Rice–Tracy’s (Eq. (27)) to 7.2% of the asymmetric 3D fracture locus (Eq. (28)). The average error of symmetric fracture locus (Eq. (29)) lies in between, and is equal to 9.3%. The geometrical representation of the asymmetric 3D fracture locus is shown in Fig. 16.

It should be noted that the material block of 2024-T351 aluminum studied by Bao is different from the one studied in the present paper for metal plasticity, and different material properties are found for these two blocks.

## 6.2. Fracture locus calibration using butterfly specimens

Fracture locus calibration using “classical specimens” is complicated and time-consuming. Another shortcoming is that the classical specimens correspond almost all to the limiting cases of loading condition ( $\bar{\theta} = 0$ , or  $\bar{\theta} = \pm 1$ ), as shown in Fig. 2. In order to obtain data points between three limiting cases, other types of specimens and tests are needed. A novel butterfly shape specimen with double curvatures, shown in Fig. 17, has been designed to calibrate the fracture locus in the space of stress triaxiality and equivalent fracture strain (Bao et al., 2004; Wierzbicki et al., 2005a; Mohr and Henn, 2004, in press). The new specimen has several advantages including the same fracture initiation location (the center of the specimen) under all loading combinations, and ability to generate a wide range of stress state using only one type of specimen. The fact that one finite element model is needed for all load conditions is removing partly the effect of mesh size. Also, this specimen is especially suited for application to metal sheets.

A710 steel is characterized by high strength and high ductility. Twenty butterfly specimens of A710 steel were machined and tested under eight loading conditions in a univer-

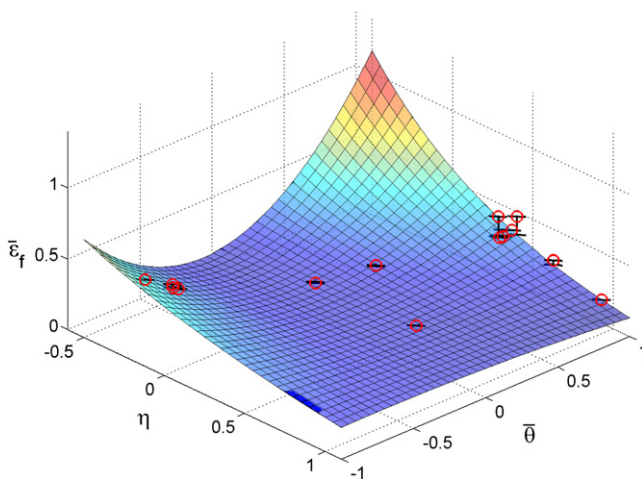


Fig. 16. 3D fracture locus of 2024-T351 aluminum (experimental data after Bao (2003), Wierzbicki et al. (2005b)).



Fig. 17. A new type of butterfly shape specimen (A710 steel).

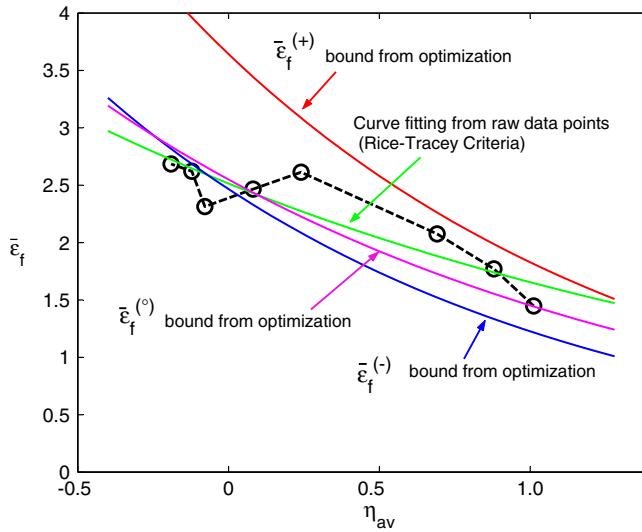


Fig. 18. Fracture locus of A710 steel in the space of stress triaxiality and fracture strain (experimental data from the Table 3 of Wierzbicki et al., 2005a).

sal biaxial testing device (UBTD, see Mohr and Doyoyo, 2004) working in conjunction the MTS testing machine. A detailed description of these tests is given in Bao et al. (2004). From the numerical simulations combined with experiment results, the fracture locus was plotted in the plane of stress triaxiality and equivalent fracture strain, as shown in Fig. 18. From the simulations, one can also get the loading conditions in the plane of stress triaxiality and the Lode angle parameter, as shown in Fig. 19. Details about the data points can be found in the Table 3 of Ref. (Wierzbicki et al., 2005a). The first approximation is to fit the data points using Rice–Tracey criteria, as shown in Fig. 18, which gives

$$\bar{\epsilon}_f = 2.5144e^{-0.4185\eta}. \quad (30)$$

The corresponding average error of Rice–Tracey criteria (Eq. (30)) is 6.7%. Similar to Section 6.1, surface fitting of these eight data points gives three bound limits, as shown in Fig. 18, and the 3D fracture locus is constructed as follows:

$$\begin{aligned} \hat{\epsilon}_f(\eta, \bar{\theta}) = & \left[ \frac{1}{2} (3.6421e^{-0.6892\eta} + 2.4659e^{-0.6986\eta}) - 2.5492e^{-0.5627\eta} \right] \bar{\theta}^2 + \frac{1}{2} \\ & \times (3.6421e^{-0.6892\eta} - 2.4659e^{-0.6986\eta}) \bar{\theta} + 2.5492e^{-0.5627\eta}. \end{aligned} \quad (31)$$

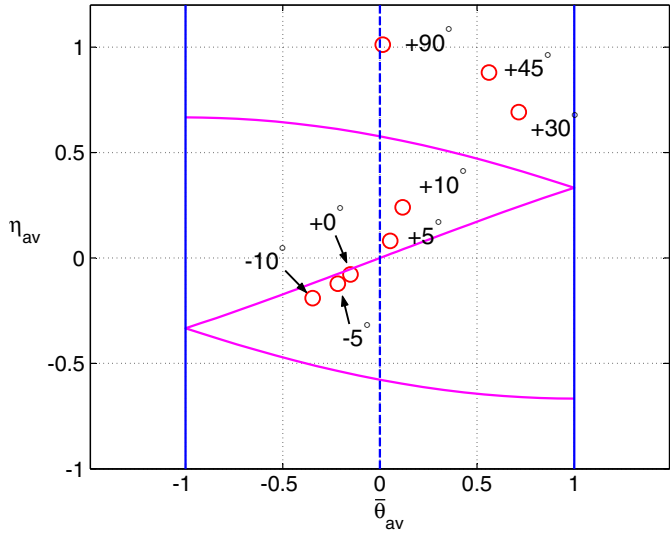


Fig. 19. Loading conditions of A710 steel in the plane of stress triaxiality  $\eta$  and the Lode angle parameter  $\bar{\theta}$  (experimental data from Wierzbicki et al., 2005a).

This 3D fracture locus with the data points is shown in Fig. 20. Compared with Eq. (30), the 3D fracture locus, Eq. (31) makes the average error decrease from 6.7% to 3.0%. The differences between the model and the experimental value are also marked in Fig. 20. One can note that  $\bar{\epsilon}_f^{(+)} \neq \bar{\epsilon}_f^{(-)}$  indicates an asymmetric fracture locus. If a symmetric fracture locus (Eq. (24)) is used in the surface fitting process, then a symmetric fracture locus is obtained as follows:

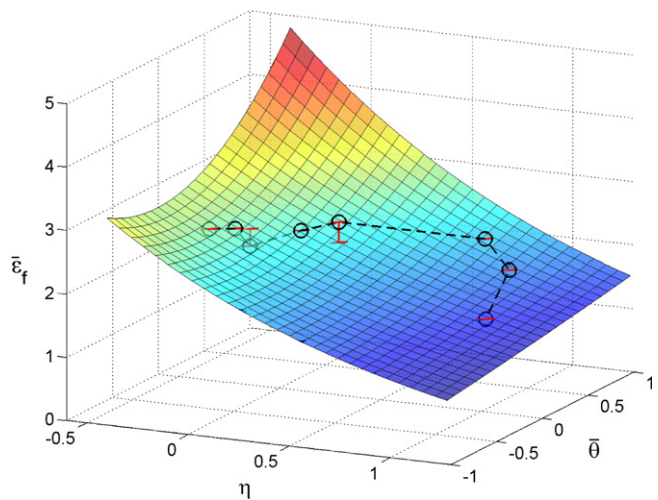


Fig. 20. 3D Fracture locus of A710 steel in the space of stress triaxiality  $\eta$ , the Lode angle parameter  $\bar{\theta}$  and fracture strain  $\bar{\epsilon}_f$  (experimental data from Wierzbicki et al., 2005a).

$$\bar{\epsilon}_f = (3.2050e^{-0.400\eta} - 2.4283e^{-0.5117\eta})\bar{\theta}^2 + 2.4283e^{-0.5117\eta}. \quad (32)$$

The corresponding average error of symmetric fracture locus (Eq. (32)) is 4.5%, which is between the Rice–Tracey’s and the asymmetric fracture locus.

## 7. Damage evolution rule

Besides the fracture locus, discussed extensively in the preceding section, the rule of damage evolution is an integral part of the fracture predictive technology. Here, a linear incremental relationship is assumed between the damage indicator  $D$  and the equivalent plastic strain  $\bar{\epsilon}_p$ ,

$$D(\bar{\epsilon}_p) = \int_0^{\bar{\epsilon}_p} \frac{d\bar{\epsilon}_p}{f(\eta, \bar{\theta})}, \quad (33)$$

where the stress state parameters  $\eta(\bar{\epsilon}_p)$ ,  $\bar{\theta}(\bar{\epsilon}_p)$  are unique functions of the equivalent plastic strain. A material element is considered to fail when the limit of ductility is reached,  $\bar{\epsilon}_p = \bar{\epsilon}_f$ , so that  $D(\bar{\epsilon}_f) = D_c = 1$ . In the limiting case (for example proportional loading), when the parameters  $(\eta, \bar{\theta})$  are constant over the loading cycle, Eq. (33) can be integrated to give

$$\bar{\epsilon}_f = f(\eta, \bar{\theta}) = \hat{\epsilon}_f(\eta, \bar{\theta}), \quad (34)$$

which reduces to the 3D fracture locus  $\hat{\epsilon}_f(\eta, \bar{\theta})$ . However, in most tests on various types of specimens, the stress state parameters  $(\eta, \bar{\theta})$  are variable. The shape of the fracture locus will then depend on whether the initial, final or some average value of these parameters is considered.

The above discussion emphasized the intrinsic difficulty in constructing a unique fracture locus. In this paper, it is proposed to determine the fracture locus based on the average value of the parameters  $(\eta, \bar{\theta})$  in the loading process.

$$\eta_{av} = \frac{1}{\bar{\epsilon}_f} \int_0^{\bar{\epsilon}_f} \eta(\bar{\epsilon}_p) d\bar{\epsilon}_p, \quad \bar{\theta}_{av} = \frac{1}{\bar{\epsilon}_f} \int_0^{\bar{\epsilon}_f} \bar{\theta}(\bar{\epsilon}_p) d\bar{\epsilon}_p. \quad (35)$$

The function  $\eta(\bar{\epsilon}_p)$  and  $\bar{\theta}(\bar{\epsilon}_p)$  are known from the numerical simulation of the tests and the equivalent strain to fracture  $\bar{\epsilon}_f$  is determined from mapping of the measured displacement to fracture into calculated strain to fracture. In all the calibration efforts presented in the preceding section, the average parameters  $(\eta_{av}, \bar{\theta}_{av})$ , defined by Eq. (35) were used. The 3D fracture locus constructed on the bases of the average values is then used as a reference surface for more complex loading paths.

## 8. Discussion and conclusion

Classical metal plasticity J2 theory assumes that the hydrostatic pressure has no effect or negligible effect on the material strain hardening, and that the flow stress is independent of the third deviatoric stress invariant (or Lode angle parameter). However, new experiments coupled with numerical simulations have shown that both the pressure effect and the effect of the third deviatoric stress invariant should be included in the metal plasticity. A new form of an asymmetric metal plasticity model, considering both these two effects, is



postulated. Calibration methods are discussed. Experimental results on aluminum 2024-T351 validated the new plasticity model.

From the similarity between yielding surface and fracture locus, the asymmetric 3D fracture locus, in the space of equivalent fracture strain  $\bar{\epsilon}_f$ , stress triaxiality  $\eta$  and the Lode angle parameter  $\bar{\theta}$ , is developed. Two methods of calibration of the fracture locus are suggested and discussed. One uses “classical” specimens and tests, another one uses the newly designed butterfly specimen under biaxial testing. The test results of Bao (2003) on aluminum 2024-T351 and the data points of A710 steel validated the postulated 3D asymmetric fracture locus.

The work in this paper proposes an extension to the classical metal plasticity and ductile fracture locus, but this extension may not be necessary for all metal materials. For example, the 1045 steel shows no obvious effect of hydrostatic pressure and Lode angle dependence on metal plasticity (Bai et al., 2006b), and the DH36 steel shows no apparent dependence on the Lode angle parameter on the fracture locus (Bai et al., 2006b). Hence, every material needs a careful executed calibration procedure with regards to both plasticity and fracture. A linear incremental dependence of the damage function  $D(\bar{\epsilon}_p)$  on the equivalent plastic strain (see Eq. (33)) was shown to work well for monotonic loading. In the case of reverse straining or more complicated loading paths, a nonlinear incremental rule must be considered (Bai et al., 2006a). This is the subject of ongoing research.

## Acknowledgements

Thanks due to Dr. Xiaoqing Teng for valuable discussions, and to Professor R.M. Brannon of the University of Utah for providing us with valuable comments. We greatly appreciate the Altair Company for the continuous support with the program HyperMesh. The financial support of this work through the NSF/Sandia Alliance program is gratefully acknowledged.

## References

- Bai, Y., Bao, Y., Wierzbicki, T., 2006a. Fracture of prismatic aluminum tubes under reverse straining. *International Journal of Impact Engineering* 32 (5), 671–701.
- Bai, Y., Teng, X., Wierzbicki, T., 2006b. Study on the effect of the third stress invariant on ductile fracture, report 151. Technical report, Impact and Crashworthiness Laboratory, Massachusetts Institute of Technology, Cambridge, MA.
- Bao, Y., 2003. Prediction of ductile crack formation in uncracked bodies. PhD Thesis, Massachusetts Institute of Technology.
- Bao, Y., Wierzbicki, T., 2004. On fracture locus in the equivalent strain and stress triaxiality space. *International Journal of Mechanical Sciences* 46 (1), 81–98.
- Bao, Y., Bai, Y., Wierzbicki, T., 2004. Calibration of a710 steel for fracture, report 135. Technical report, Impact and Crashworthiness Laboratory, Massachusetts Institute of Technology, Cambridge, MA.
- Bardet, J., 1990. Lode dependences for isotropic pressure-sensitive elastoplastic materials. *Journal of Applied Mechanics, Transactions ASME* 57 (3), 498–506, ISSN: 0021-8936.
- Barlat, F., Lege, D.J., Brem, J.C., 1991. A six-component yield function for anisotropic materials. *International Journal of Plasticity* 7 (7), 693–712.
- Barlat, F., Becker, R.C., Hayashida, Y., Maeda, Y., Yanagawa, M., Chung, K., Brem, J.C., Lege, D.J., Matsui, K., Murtha, S.J., Hattori, S., 1997. Yielding description for solution strengthened aluminum alloys. *International Journal of Plasticity* 13 (4), 385–401.
- Barlat, F., Aretz, H., Yoon, J., Karabin, M., Brem, J., Dick, R., 2005. Linear transformation-based anisotropic yield functions. *International Journal of Plasticity* 21 (5), 1009–1039.



- Bigoni, D., Piccolroza, A., 2003. A new yield function for geomaterials. In: C. Viggiani (Ed.), *Constitutive Modeling and Analysis of Boundary Value Problems in Geotechnical Engineering*, Napoli, pp. 266–281.
- Bridgman, P.W., 1952. *Studies in Large Plastic Flow and Fracture*. McGraw-Hill, New York.
- Brownrigg, A., Spitzig, W.A., Richmond, O., Teirlinck, D., Embury, J.D., 1983. The influence of hydrostatic pressure on the flow stress and ductility of a spheroidized 1045 steel. *Acta Metallurgica* 31 (8), 1141–1150.
- Brüning, M., 1999. Numerical simulation of the large elastic–plastic deformation behavior of hydrostatic stress-sensitive solids. *International Journal of Plasticity* 15 (11), 1237–1264.
- Cazacu, O., Barlat, F., 2004. A criterion for description of anisotropy and yield differential effects in pressure-insensitive metals. *International Journal of Plasticity* 20 (11), 2027–2045.
- Cazacu, O., Plunkett, B., Barlat, F., 2006. Orthotropic yield criterion for hexagonal closed packed metals. *International Journal of Plasticity* 22 (7), 1171–1194.
- Drucker, D., Prager, W., 1952. Soil mechanics and plastic analysis or limit design. *Quarterly of Applied Mathematics* 10, 157–165.
- El-Magd, E., Gese, H., Tham, R., Hooputra, H., Werner, H., 2001. Fracture criteria for automobile crashworthiness simulation of wrought aluminium alloy components. *Materialwissenschaft und Werkstofftechnik* 32, 712–724.
- Fossum, A., Brannon, R., 2006. On a viscoplastic model for rocks with mechanism-dependent characteristic times. *Acta Geotechnica* 1, 89–106.
- Gao, X., Kim, J., 2006. Modeling of ductile fracture: significance of void coalescence. *International Journal of Solids and Structures* 43, 6277–6293.
- Gurson, A.L., 1975. Plastic flow and fracture behavior of ductile materials incorporating void nucleation, growth and interaction. PhD Thesis, Brown University.
- Han, D.J., Chen, W.F., 1985. A nonuniform hardening plasticity model for concrete materials. *Mechanics of Materials* 4 (3–4), 283–302.
- Hancock, J.W., Brown, D.K., 1983. On the role of strain and stress state in ductile failure. *Journal of the Mechanics and Physics of Solids* 31 (1), 1–24.
- Hancock, J.W., Mackenzie, A.C., 1976. On the mechanisms of ductile failure in high-strength steels subjected to multi-axial stress-states. *Journal of the Mechanics and Physics of Solids* 24 (2–3), 147–160.
- Hosford, W.F., 1972. A generalized isotropic yield criterion. *Journal of Applied Mechanics* 39, 607.
- Johnson, G.R., Cook, W.H., 1985. Fracture characteristics of three metals subjected to various strains, strain rates, temperatures and pressures. *Engineering Fracture Mechanics* 21 (1), 31–48.
- Kamoulakos, A., Culiére, P., Araki, T., 2003. Prediction of ductile metal rupture with the e-w model in pam-crash. In: *IBEC 2003 Chiba, Japan*.
- Karafilis, A.P., Boyce, M.C., 1993. A general anisotropic yield criterion using bounds and a transformation weighting tensor. *Journal of the Mechanics and Physics of Solids* 41 (12), 1859–1886.
- Karr, D.G., Law, F.P., Fatt, M.H., Cox, G.F.N., 1989. Asymptotic and quadratic failure criteria for anisotropic materials. *International Journal of Plasticity* 5 (4), 303–336.
- Khan, A.S., Jackson, K.M., 1999. On the evolution of isotropic and kinematic hardening with finite plastic deformation. Part I: compression/tension loading of OFHC copper cylinders. *International Journal of Plasticity* 15 (12), 1265–1275.
- Kuroda, M., 2004. A phenomenological plasticity model accounting for hydrostatic stress-sensitivity and vertex-type of effect. *Mechanics of Materials* 36 (3), 285–297.
- Mackenzie, A.C., Hancock, J.W., Brown, D.K., 1977. On the influence of state of stress on ductile failure initiation in high strength steels. *Engineering Fracture Mechanics* 9 (1), 167–168.
- Malvern, L.E., 1969. *Introduction to the Mechanics of a Continuous Medium*. Prentice-Hall, Inc.
- McClintock, F.A., 1968. A criterion of ductile fracture by the growth of holes. *Journal of Applied Mechanics* 35, 363–371.
- Menetrey, P., Willam, K., 1995. Triaxial failure criterion for concrete and its generalization. *ACI Structural Journal* 92, 311–318.
- Mises, R.V., 1913. *Mechanik der festem Koeper im plastisch deformablem Zustand*, Goettingen Nachrichten. Math. Phys. Klasse 4, 582–592.
- Mohr, D., Doyoyo, M., 2004. Experimental investigation on the plasticity of hexagonal aluminum honeycomb under multiaxial loading. *Journal of Applied Mechanics* (3), 375–385.

- Mohr, D., Henn, S., 2004. A New Method for Calibrating Phenomenological Crack Formation Criteria, report 113. Technical report, Impact and Crashworthiness Laboratory, Massachusetts Institute of Technology, Cambridge, MA.
- Mohr, D., Henn, S., in press. Calibration of stress-triaxiality dependent crack formation criteria: a new hybrid experimental–numerical method. *Experimental Mechanics*, doi:10.1007/s11340-007-9039-7.
- Needleman, A., Tvergaard, V., 1984. An analysis of ductile rupture in notched bars. *Journal of the Mechanics and Physics of Solids* 32 (6), 461–490.
- Rachlerla, V., Bassani, J., 2007. Strain burst phenomena in the necking of a sheet that deforms by non-associated plastic flow. *Modelling and Simulation in Materials Science and Engineering* 15, S297–S311.
- Rice, J.R., Tracey, D.M., 1969. On the ductile enlargement of voids in triaxial stress fields. *Journal of the Mechanics and Physics of Solids* 17, 201–217.
- Richmond, O., Spitzig, W.A., 1980. Pressure dependence and dilatancy of plastic flow. In: *Theoretical and Applied Mechanics, Proceedings of the 15th International Congress of Theoretical and Applied Mechanics*, Toronto, Ont., Canada. North-Holland Publ. Co., Amsterdam, The Netherlands, pp. 377–386.
- Spitzig, W.A., Richmond, O., 1984. The effect of pressure on the flow stress of metals. *Acta Metallurgica* 32 (3), 457–463.
- Tresca, H., 1864. *Comptes Rendus de l'Academie Des Sciences Serie* 59, 754.
- Vegter, H., van den Boogaard, A., 2006. A plane stress yield function for anisotropic sheet material by interpolation of biaxial stress states. *International Journal of Plasticity* 22 (3), 557–580.
- Wierzbicki, T., Xue, L., 2005. On the effect of the third invariant of the stress deviator on ductile fracture. Technical report, Impact and Crashworthiness Laboratory, Massachusetts Institute of Technology, Cambridge, MA.
- Wierzbicki, T., Bao, Y., Bai, Y., 2005a. A new experimental technique for constructing a fracture envelope of metals under multi-axial loading. In: *Proceedings of the 2005 SEM Annual Conference and Exposition on Experimental and Applied Mechanics*, pp. 1295–1303.
- Wierzbicki, T., Bao, Y., Lee, Y.-W., Bai, Y., 2005b. Calibration and evaluation of seven fracture models. *International Journal of Mechanical Sciences* 47 (4–5), 719–743.
- Wilkins, M.L., Streit, R.D., Reaugh, J.E., 1980. Cumulative-strain-damage model of ductile fracture: simulation and prediction of engineering fracture tests, ucrl-53058. Technical report, Lawrence Livermore Laboratory, Livermore, CA.
- Wilson, C.D., 2002. A critical reexamination of classical metal plasticity. *Journal of Applied Mechanics, Transactions ASME* 69 (1), 63–68, ISSN: 0021-8936.
- Xu, B., Liu, X., 1995. *Applied Mechanics: Elasticity and Plasticity*. Tsinghua University Press, Beijing, China.
- Xue, L., 2007. Damage accumulation and fracture initiation in uncracked ductile solids subject to triaxial loading. *International Journal of Solids and Structures* 44 (16), 5163–5181.
- Zhang, K.S., Bai, J.B., Francois, D., 2001. Numerical analysis of the influence of the lode parameter on void growth. *International Journal of Solids and Structures* 38 (32–33), 5847–5856.